

LETTER TO THE EDITOR

Searching for H_α emitting sources around MWC 758 [★]

SPHERE/ZIMPOL high-contrast imaging

N. Huélamo¹, G. Chauvin^{2,3}, H. M. Schmid⁴, S. P. Quanz⁴, E. Whelan⁵, J. Lillo-Box⁶, D. Barrado¹, B. Montesinos¹, J.M. Alcalá⁷, M. Benisty^{2,3}, I. de Gregorio-Monsalvo^{6,8}, I. Mendigutía¹, H. Bouy⁹, B. Merín¹⁰, J. de Boer¹¹, A. Garufi¹², and E. Pantin¹³

¹ Centro de Astrobiología (CSIC-INTA), Camino bajo del Castillo s/n, E-28692 Villanueva de la Cañada, Madrid, Spain
e-mail: nhuelamo@cab.inta-csic.es

² Unidad Mixta Internacional Franco-Chilena de Astronomía, CNRS/INSU UMI 3386 and Departamento de Astronomía, Universidad de Chile, Casilla 36-D, Santiago, Chile

³ Univ. Grenoble Alpes, CNRS, IPAG, F-38000 Grenoble, France

⁴ ETH Zurich, Institute of Particle Physics and Astrophysics, Wolfgang-Pauli-Strasse 27, 8093 Zurich, Switzerland

⁵ Maynooth University Department of Experimental Physics, National University of Ireland, Maynooth Co. Kildare, Ireland

⁶ European Southern Observatory, Alonso de Cordova 3107, Casilla 19, Vitacura, Santiago, Chile

⁷ INAF-Osservatorio Astronomico di Capodimonte, via Moiariello 16, 80131 Napoli, Italy

⁸ Joint ALMA Observatory, Alonso de Córdova 3107, Vitacura, Santiago, Chile

⁹ Laboratoire d'Astrophysique de Bordeaux, Univ. Bordeaux, CNRS, B18N, allée Geoffroy Saint-Hilaire, 33615 Pessac, France

¹⁰ ESAC Science Data Centre, ESA-ESAC, Spain

¹¹ Leiden Observatory, Leiden University, PO Box 9513, 2300 RA Leiden, The Netherlands

¹² Universidad Autónoma de Madrid, Dpto. Física Teórica, Madrid, Spain

¹³ Laboratoire AIM, CEA/DRF, CNRS, Université Paris Diderot, IRFU/DAS, F-91191 Gif sur Yvette, France

Received ; accepted

ABSTRACT

Context. MWC 758 is a young star surrounded by a transitional disk. The disk shows an inner cavity and spiral arms that could be caused by the presence of protoplanets. Recently, a protoplanet candidate has been detected around MWC 758 through high-resolution L' -band observations. The candidate is located inside the disk cavity at a separation of ~ 111 mas from the central star, and at an average position angle of $\sim 165.5^\circ$.

Aims. We aim at detecting accreting protoplanet candidates within the disk of MWC 758 through spectral angular differential imaging observations in the optical regime. In particular, we explore the emission at the position of the detected planet candidate.

Methods. We have performed simultaneous adaptive optics observations in the H_α line and the adjacent continuum using SPHERE/ZIMPOL at the Very Large Telescope (VLT).

Results. The data analysis does not reveal any H_α signal around the target. The derived contrast curve in the B_Ha filter allows us to derive a 5σ upper limit of ~ 7.6 mag at 111 mas, the separation of the previously detected planet candidate. This contrast translates into a H_α line luminosity of $L_{H_\alpha} \lesssim 5 \times 10^{-5} L_\odot$ at 111 mas. Assuming that L_{H_α} scales with L_{acc} as in Classical T Tauri stars as a first approximation, we can estimate an accretion luminosity of $L_{acc} < 3.7 \times 10^{-4} L_\odot$ for the protoplanet candidate. For the predicted mass range of MWC 758b, $0.5\text{--}5 M_{Jup}$, this implies accretion rates smaller than $\dot{M} < 3.4 \times (10^{-8}\text{--}10^{-9}) M_\odot/\text{yr}$, for an average planet radius of $1.1 R_{Jup}$. Therefore, our estimates are consistent with the predictions of accreting circumplanetary accretion models for $R_{in} = 1 R_{Jup}$. The ZIMPOL line luminosity is consistent with the H_α upper limit predicted by these models for truncation radii $\lesssim 3.2 R_{Jup}$.

Conclusions. The non-detection of any H_α emitting source in the ZIMPOL images does not allow us to unveil the nature of the L' detected source. Either it is a protoplanet candidate or a disk asymmetry.

Key words. stars: pre-main sequence – stars: planetary systems – stars: individual: MWC 758 – accretion, accretion disks

1. Introduction

The study of transitional disks is an important tool to understand planet formation and evolution. High-angular-resolution observations of these disks at different wavelengths have revealed structures including spiral arms, warps, gaps and radial streams that might be related to on-going planet formation (e.g. Andrews et al. 2011; Mayama et al. 2012; Grady et al. 2013; Boccaletti et al. 2013; Pinilla et al. 2015; Pérez et al. 2016; Mendigutía

et al. 2017; Pohl et al. 2017). Therefore, a great effort has been made to detect protoplanets still embedded in these disks (e.g. Huélamo et al. 2011; Kraus & Ireland 2012; Quanz et al. 2013; Biller et al. 2014; Close et al. 2014; Whelan et al. 2015; Sallum et al. 2015), since they can shed light on the planet formation mechanisms, the required physical conditions, and the physics of gas accretion to form the atmospheres of giant planets.

In this context, MWC 758 (HD 36112, HIP25793) is an interesting target to study planet formation. The object is a young (3 ± 2 Myr, Meeus et al. 2012) Herbig Ae star. While the *Hip-parcos* parallax provided a distance of 279^{+94}_{-58} pc (van Leeuwen

[★] Based on observations obtained at Paranal Observatory under program 096.C-0267(A) and 96.C-0248(A).

2007), the *GAIA* TGAS Catalog reports a parallax of 6.63 ± 0.38 mas, resulting in a distance of 151_{-8}^{+10} pc (Gaia Collaboration et al. 2016a,b).

MWC 758 is surrounded by a transitional disk spatially resolved at infrared (IR) and sub-millimeter (sub-mm) wavelengths (Chapillon et al. 2008; Isella et al. 2010; Andrews et al. 2011; Grady et al. 2013; Marino et al. 2015). The disk inclination is $21 \pm 2^\circ$, and it shows several structures and a marginally resolved cavity. Benisty et al. (2015) presented SPHERE/IRDIS IR polarimetric observations of the source in the Y-band ($1.04 \mu\text{m}$). The unprecedented angular resolution of these observations allowed them to spatially resolve several non-axisymmetric features down to 26 au (~ 14 au with the new *GAIA* distance), and a no fully depleted cavity. They also resolved the two spiral arms previously reported by Grady et al. (2013) through HiCIAO observations. They presented a model that concludes that the presence of planets inside the cavity cannot reproduce the large opening angle of the spirals. On the other hand, models with an outer companion could work better to explain these disk structures (see e.g. Dong et al. 2015). More recently, Boehler et al. (2017) presented new sub-mm ALMA data showing a large dust cavity of ~ 40 au in radius, evidence of a warped inner disk, and the presence of two dust clumps in the outer regions of the disk. To explain the whole disk structure, they propose the presence of two giant planets, one in the inner regions responsible for carving the cavity, and an outer one responsible for the spirals.

Interestingly, Reggiani et al. (2017) reported the presence of a point-like source inside the sub-mm cavity, at a separation of $\sim 111 \pm 4$ mas from the central star. The object was detected in the L-band at two different epochs, with a contrast of $\Delta L = 7.0 \pm 0.3$ mag with respect to the primary. As the authors explain, this emission could be caused by an embedded protoplanet, although they cannot exclude that it is associated with an asymmetric disk feature. The comparison of their observations with circumplanetary disk accretion models (Zhu 2015) are consistent with a $0.5\text{-}5 M_{\text{Jup}}$ planet accreting at a rate of $10^{-7}\text{-}10^{-9} M_{\odot}/\text{yr}$.

We have explored the possibility of detecting protoplanet candidates using the H_{α} emission line as an accretion tracer (see e.g. Close et al. 2014; Sallum et al. 2015). In this letter, we present spectral angular differential imaging observations of MWC 758 obtained with SPHERE/ZIMPOL at the Very Large Telescope (VLT). We used two filters, one centered at the H_{α} line, and the other one at the adjacent continuum. We complemented the ZIMPOL data with optical spectroscopy using the CAFE spectrograph at the 2.2m telescope in the Calar Alto observatory. MWC 758 was part of a program to detect young accreting protoplanets within the circumstellar disks of young stars.

2. Observations and data reduction

2.1. VLT/ZIMPOL

The SPHERE Open Time observations (096.C-0267.A) were obtained on December 30, 2015. The ZIMPOL instrument of SPHERE (Beuzit et al. 2008; Thalmann et al. 2008) was used in spectral and angular differential imaging modes (Marois et al. 2006; Racine et al. 1999). In addition to the pupil stabilized mode, ZIMPOL simultaneously imaged MWC 758 in two different filters: B_Ha ($\lambda_c = 655.6$ nm and $\Delta\lambda = 5.5$ nm) and Cnt_Ha ($\lambda_c = 644.9$ nm and $\Delta\lambda = 4.1$ nm). We obtained 190 individual exposures of 60 seconds each, resulting in a total exposure time of ~ 3 hours on-source (from 02:20 UT to 05:24 UT). The condi-

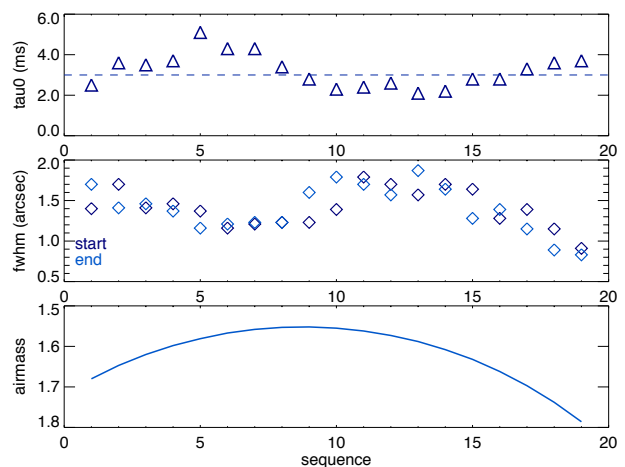


Fig. 1. Average atmospheric conditions during the ZIMPOL observations. The x-axis shows the average conditions in cycles of 10 mins. Therefore, we have represented 19 cycles of 10 mins each. From top to bottom, we have plotted the coherence time (τ_0), the average FWHM as seen by the guide probe at the beginning and end of the cycles, and the airmass.

tions were photometric until 03:39 (UT) when they turned into clear.

The observing conditions (monitored by the seeing and coherence time) were variable during the complete observing sequence. The seeing varied between $0''.7$ and $2''.0$, and the coherence time between 5 ms and 2 ms (see Fig 1) affecting the final Adaptive Optics (AO) correction of the ZIMPOL images. Figure 2 shows the maximum counts registered on the target (good proxy for the Strehl variation in photometric/clear conditions) throughout the 190 individual images in the B_Ha filter (the same variations are observed in Cnt_Ha). The mean full-width at half-maximum (FWHM) measured in the individual images is ~ 9 pixels, that is, ~ 32 mas considering the pixel scale of 3.6 mas/pixel of the ZIMPOL detector.

The data reduction was performed using a customary pipeline developed by our team. As a first step, the data were bias-subtracted, flat-fielded, and bad-pixel corrected. Subsequently, the individual images were recentered using a simple Moffat function to estimate the centroid position as no coronagraph was used. For the point-spread function (PSF) subtraction, the individual filter datasets (B_Ha and Cnt_Ha) were considered separately to apply a standard Angular Differential Imaging (ADI) processing technique using classical and smart-ADI (cADI and sADI; Lafrenière et al. 2007; Chauvin et al. 2012) and principal component analysis (PCA) (Soummer et al. 2012). For the B_Ha-Cnt_Ha spectral and angular differential imaging processing, the individual Cnt_Ha images were first spatially rescaled to the B_Ha filter resolution, then flux-normalized considering the total flux ratio between B_Ha and Cnt_Ha within an aperture of $r = 10$ pixels, before finally applying the subtraction B_Ha-Cnt_Ha frame per frame to exploit the simultaneity of both observations. ADI processing in cADI, sADI and PCA was then applied to the resulting differential datacube.

The ADI detection limits were then estimated from a standard pixel-to-pixel noise map of each filter within a box of 5×5 pixels sliding from the star to the limit of the ZIMPOL field of view. The contrast curves at 5σ were then obtained using the pixel-to-pixel noise map divided by the ADI flux loss, and corrected from small number statistics following the prescription

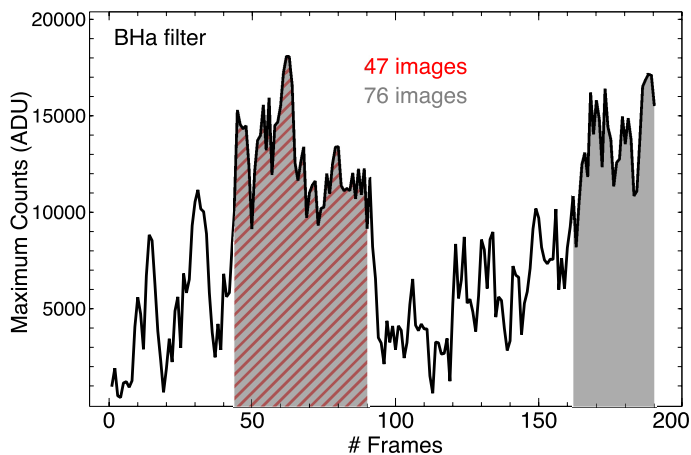


Fig. 2. The maximum counts (in ADU) measured in the 190 individual frames obtained in the B_Ha filter. The gray shaded areas correspond to the 76 selected images (see text), while the hatched red area corresponds to the best 47 individual exposures.

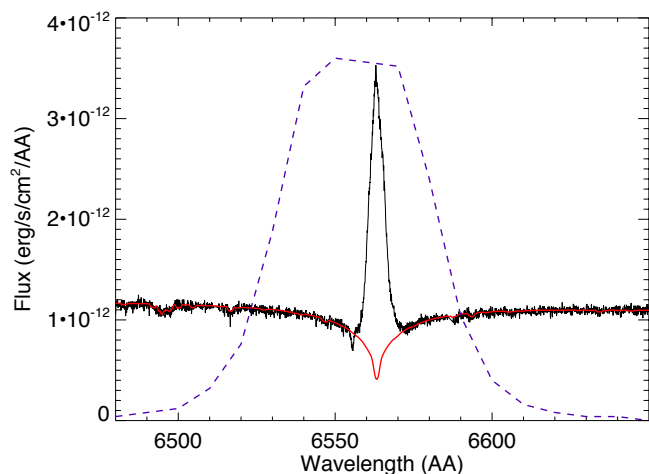


Fig. 3. The observed CAFE/CAHA spectrum around the H_α line (in black). The red line represents the model used to fit the stellar atmosphere (see text). The dashed blue line represents the ZIMPOL B_Ha filter transmission curve.

of Mawet et al. (2014) adapted to our 5σ confidence level at small angles with ZIMPOL. The same method was applied for the differential imaging dataset to illustrate the gain in speckle subtraction in the inner region below 200 mas.

Finally, and to consider the impact of variable atmospheric conditions, we analyzed three different datasets (see Figure 2): first, we worked with the whole observing sequence (190 images) which covers a field rotation of ~ 55 degrees; second, we selected the best AO-corrected images through the whole exposure (images 44 to 90, and 162 to 190, a total of 76 frames, covering 15 deg and 7 deg of field rotation, respectively) and, third, we kept the 47 images with the best AO correction in the first half of the observing sequence (images 44 to 90, ~ 15 deg of field rotation). We finally worked with the latest dataset (47 individual images) to achieve the best detection performances at close separations. The average Strehl ratio of this dataset is $\sim 10\%$.

2.2. CAHA/CAFE spectroscopy

To complement the SPHERE/ZIMPOL observations, we performed high-resolution spectroscopy of MWC 758 with the CAFE spectrograph attached to the 2.2m telescope in the Calar Alto Observatory (Aceituno et al. 2013). CAFE is equipped with a $2''4$ diameter optical fibre, and provides high-resolution spectra ($R \sim 63\,000$) over the 3900-9600 Å spectral range.

We obtained a spectrum on the night of December 24 2015 under photometric conditions and with an average seeing of $0''.7$. The total exposure time was 600 seconds. The spectrum was reduced with a dedicated pipeline developed by the observatory and explained in Aceituno et al. (2013). The processing was as follows: the data were bias subtracted and flat-field corrected. We used thorium-argon (ThAr) exposures obtained after the science spectrum to wavelength-calibrate the data. The spectrum was flux-calibrated using the standard star HD19445, observed one hour before the science target with an airmass difference of ~ 0.2 . We compared the calibrated spectrum with published photometry (Beskrovnaya et al. 1999), obtaining that the spectrum is ~ 1.2 times brighter (0.2 mag) in the R-band. Therefore, we estimate a precision in the flux calibration of $\sim 20\%$ in this band.

Figure 3 shows a portion of the calibrated CAFE spectrum containing the H_α line. We measure a line flux of $1.3 \pm 0.3 \times 10^{-11}$ erg/s/cm 2 . To correct for the stellar photospheric absorption, we first computed synthetic spectra using the codes ATLAS and SYNTH (Kurucz 1993) fed with the models describing the stratification of the stellar atmospheres (Castelli & Kurucz 2003). Solar abundances were assumed. The synthetic spectrum was computed assuming $T_{\text{eff}} = 7750$ K and $\log g_* = 4.0$ as the starting point, following the result from Beskrovnaya et al. (1999). A value of $v \sin i = 50$ km/s was adopted since it reproduces well the width of the photospheric line profiles. The model is displayed as a red line in Figure 3. The estimated H_α line flux, corrected from the photospheric absorption, is $1.6 \pm 0.3 \times 10^{-11}$ erg/s/cm 2 . Taking into account the reported visual extinction of $A_V = 0.16$ mag (Meeus et al. 2012), we can correct the flux adopting a value of $A_R \sim 0.12$ mag (Rieke & Lebofsky 1985), and estimate a line luminosity of $\sim 0.013 L_\odot$ for a distance of 151 pc.

Assuming that the Herbig Be/Ae relationship between H_α luminosity and accretion luminosity derived by Fairlamb et al. (2017) holds, we estimate $\log(L_{\text{acc}}/L_\odot) = (2.09 \pm 0.06) + (1.00 \pm 0.05) \times \log(L_{H_\alpha}/L_\odot)$. We derive $L_{\text{acc}} = 1.6 \pm 0.4 L_\odot$. Following Mendigutía et al. (2011), we estimate a mass accretion rate of $\sim (7 \pm 2) \times 10^{-8} M_\odot/\text{yr}$, for a stellar mass of $1.4 \pm 0.3 M_\odot$ and a stellar radius of $2 R_\odot$ (Boehler et al. 2017), already scaled to the GAIA distance.

Finally, we note that although the CAFE spectrum is not simultaneous to the SPHERE observations, it allows us to characterize the primary star and to double-check the calibration of our ZIMPOL data with close in-time observations.

3. Results and discussion

The SPHERE/ZIMPOL combined images of MWC 758 in the B_Ha and the Cnt_Ha filters, together with the differential B_Ha-Cnt_Ha image, are displayed in Figure 4. We show the results of combining the 47 best images. We have not detected any point-like source in any of the analyzed datasets. The 5σ contrast achieved in the two individual filters, and in the differential sequence, is displayed in Figure 5. We reach ~ 7.6 mag in the B_Ha and the Cnt_Ha filters at a separation of 111 mas, that is, where the protoplanet candidate by Reggiani et al. (2017) is detected.

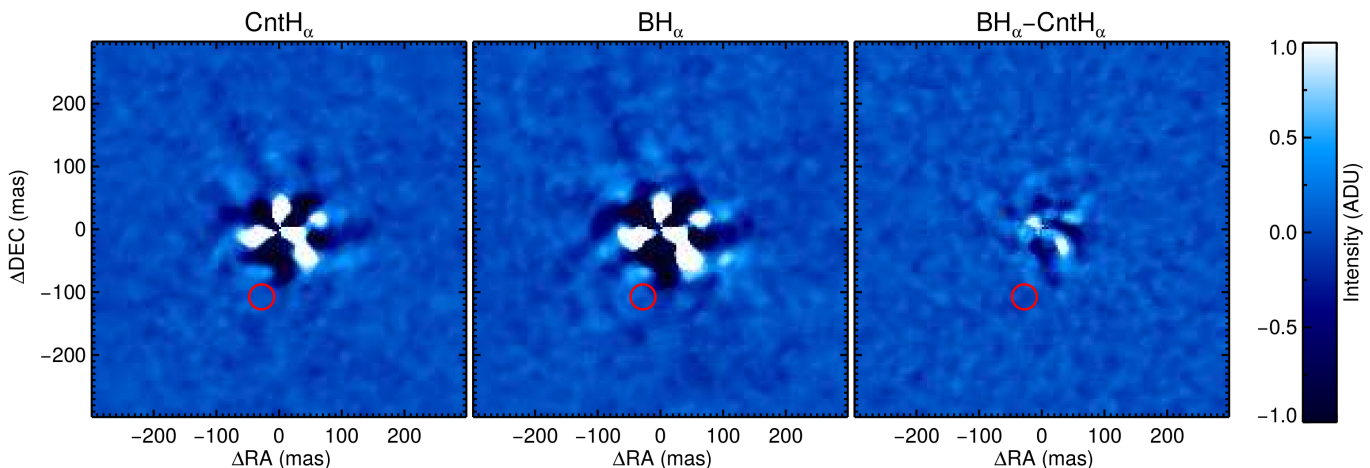


Fig. 4. VLT/ZIMPOL ADI reduced images of MWC 758 processed with PCA (5 modes) in the Cnt_Ha (left) and B_Ha (center) filters. The ASDI image (B_Ha-Cnt_Ha) processed with PCA (5 modes) is displayed in the right panel. North is up and East to the left. The red circle shows the position at a separation of 111 mas, and a PA of 165.5° , where the companion candidate was detected by [Reggiani et al. \(2017\)](#) in the L' -band.

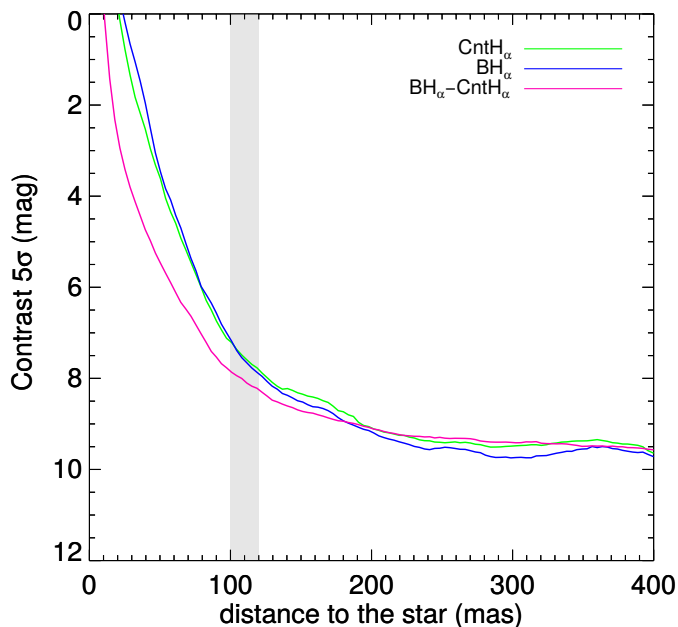


Fig. 5. VLT/ZIMPOL 5σ contrast curves obtained in Cnt_Ha and B_Ha in ADI using PCA, and in B_Ha-Cnt_Ha in ASDI using PCA. The gray area shows the position of the companion candidate detected at L' by [Reggiani et al. \(2017\)](#). The curves are derived using the best 47 images.

The fact that we do not detect any companion in the individual filters and differential images does not allow us a direct estimation of its H_α flux. However, since the 47 images were observed under photometric conditions, we can convert the B_Ha contrast curve into fluxes by calibrating the counts (cts) from the primary star. To this aim, we first performed aperture photometry of the central star in ten individual images (out of the 47), using a large aperture radius (320 pixel radius, ~ 1 arcsec). We obtain a total of $\sim 6.5(\pm 0.6) \times 10^6$ cts . The uncertainty includes a relative error of 10% associated to the channel splitting, and the

background error estimation. We converted the integrated counts into fluxes using the zero-points (ZPs) derived by [Schmid et al. \(2017\)](#), and their Eq. (4):

$$f = (cts/s) \cdot 10^{0.4(a_m \times k_1 + m_{mode})} \cdot c_{zp}^l \quad (1)$$

Assuming that all the emission in the B_Ha filter comes from the H_α line, we can convert the counts per second adopting a zero-point (c_{zp}^l) of $7.2(\pm 0.4) \times 10^{-16}$ erg/(cm^2 ct), and an m_{mode} value of -0.23 mag to take into account the usage of the R -band dichroic (Schmid, private communication). For an average airmass (a_m) of 1.57 (for the 47 images), and a typical R -band atmospheric extinction value of $k_1 \sim 0.08$ ([Patat et al. 2011](#)), we obtained a B_Ha flux of $\sim 7.1(\pm 0.8) \times 10^{-11}$ erg/s/ cm^2 for the primary star. We note that the assumption that all the counts in the B_Ha filter come from the line, results in a line flux over-estimation of a factor of ~ 5 when compared with the line flux measured directly in the spectrum.

We used the total calibrated flux in B_Ha, together with the contrast curve, to derive an upper limit ($5\text{-}\sigma$) to the B_Ha flux at different separations from the central object. In particular, we estimated a flux $< 6.2 \times 10^{-14}$ erg/s/ cm^2 at 111 mas, the separation of the planet candidate. If we assume that all the flux comes from the line, and an extinction equal to that of the primary star ($A_R = 0.12$ mag), we estimate a line luminosity of $L_{H_\alpha} < 4.9 \times 10^{-5} L_\odot$ for a distance of 151 pc. When compared with the other two H_α sources detected in transitional disks, we see that our ZIMPOL upper limit is of the same order of the emission of the protoplanet candidate LkCa15 b ($6 \times 10^{-5} L_\odot$, [Sallum et al. 2015](#)), and one order of magnitude fainter than the very low-mass star ($\sim 0.2 M_\odot$) HD142527 B ($5 \times 10^{-4} L_\odot$, [Close et al. 2014](#)). We note that the smallest and lightest accreting companions to stars in the brown dwarf/planet boundary (e.g., GQ Lup b, FW Tau b, GSC 06214–0210 b, DH Tau b) show H_α luminosity values in the range $L_{H_\alpha} \sim 2 \times 10^{-5} - 6.5 \times 10^{-7} L_\odot$ (see e.g. [Bowler et al. 2014](#); [Zhou et al. 2014](#)).

As explained in [Reggiani et al. \(2017\)](#), the mass of the companion candidate (M_p) should be below $5.5 M_{\text{Jup}}$ to allow for small dust replenishment within the disk. The comparison of their L' -band luminosity with circumplanetary accretion models ([Zhu 2015](#)) is consistent with $M_p M \sim 2(\pm 1) - 6.0(\pm 1.5) \times$

$10^{-5} M_{\text{Jup}}^2/\text{yr}$ for disk inner radii of $R_{\text{in}} = 1 - 4 R_{\text{Jup}}$, respectively (see their Fig. 6). Given the mass constraints, their data is compatible with a $0.5\text{-}5 M_{\text{Jup}}$ protoplanet with an accretion rate of $10^{-7}\text{-}10^{-9} M_\odot/\text{yr}$.

As a first approximation, and following previous works (Close et al. 2014; Sallum et al. 2015), we can estimate the accretion luminosity (L_{acc}) of MWC 758 b assuming that it scales with L_{H_α} as in Classical T Tauri stars (CTTSs). In this case, $L_{\text{acc}} = 10^{[(2.99 \pm 0.16) + (1.49 \pm 0.05) \log(L_{H_\alpha})]}$ (Rigliaco et al. 2012), and we derive an upper limit of $L_{\text{acc}} < 3.7 \times 10^{-4} L_\odot$ at 111 mas. Using the L_{acc} upper limit, and following Gullbring et al. (1998), we estimate $M_p \dot{M} < 1.8 \times 10^{-5} M_{\text{Jup}}^2/\text{yr}$, assuming a planet radius of $1.1 R_{\text{Jup}}$ (the average value for $0.5\text{-}5 M_{\text{Jup}}$ planets according to 3 Myr COND models, Baraffe et al. 2003). This upper limit is consistent with the lowest values of $M_p \dot{M}$ derived for $R_{\text{in}} = 1 R_{\text{Jup}}$ by Reggiani et al. (2017). If we assume planet masses of $0.5\text{-}5 M_{\text{Jup}}$ and a planet radius of $1.1 R_{\text{Jup}}$, we estimate accretion rates of $\dot{M} < 3.4 \times (10^{-8} - 10^{-9}) M_\odot/\text{yr}$ for MWC 758 b.

We note, however, that low-mass brown dwarfs and planetary mass objects seem not to follow the $L_{H_\alpha} - L_{\text{acc}}$ relation derived for CTTSs: as an example, Zhou et al. (2014) estimated the accretion rates of three very low-mass substellar sources through their UV/optical excesses, and found values more than one order of magnitude higher than the values expected from extrapolating the CTTSs relationship. Interestingly, they also show that, in contrast with young TTSs, very low-mass accreting objects might emit a larger fraction of their accretion luminosity in the H_α line.

An alternative way to study the H_α emission of protoplanets is to compare their estimated luminosity with predictions from accreting circumplanetary models (Zhu 2015). In this latter work, the author studied the expected H_α emission from protoplanets due to magnetospheric accretion (see their Eq. 22), obtaining upper limits to their L_{H_α} luminosity three orders of magnitude lower than the typical values derived for CTTSs ($\sim 5 \times 10^{-3} L_\odot$, Rigliaco et al. 2012). The line luminosity depends on the truncation radius of the inner disk, and the infall velocity of the accreted material. According to their Eq. 22, our ZIMPOL data ($L_{H_\alpha} \lesssim 5 \times 10^{-5} L_\odot$) is consistent with their predicted luminosity for truncation radii smaller than $\sim 3.2 R_{\text{Jup}}$.

The fact that we do not detect any source in the B_H filter might suggest that the MWC 758 protoplanet candidate is accreting at a low rate and we are not sensitive to its $H\alpha$ emission. Another possibility is that the object is undergoing episodic accretion and we have observed it in a quiescent state. Although the disk inclination is closer to face-on, the sub-mm cavity is filled with small grains (Benisty et al. 2015), so the object might also be too extincted and therefore undetectable in the optical regime. Finally, we cannot exclude the possibility that the L' infrared emission is related to a disk asymmetry and not with a protoplanet, as proposed by Reggiani et al. (2017). In fact, it is known that ADI techniques can highlight disk features in such a way that they can look like planets, especially for low-inclination systems (see e.g. Ligi et al. 2018). Follow-up L' observations, together with deeper K -band data, will help to understand the true nature of the infrared detection.

Acknowledgements. We are grateful to the referee, C. Grady, whose comments helped to improve this manuscript. This research has been funded by Spanish grants ESP2015-65712-C5-1-R and ESP2017-87676-C5-1-R. NH is indebted to the Paranal staff that gave their support during the observations, and to the CAHA staff. Part of this work has been carried out within the framework of the National Centre for Competence in Research PlanetS supported by the Swiss National Science Foundation. S.P.Q. and H.M.S. acknowledge the financial support of the SNSF. JMA acknowledge financial support from the project PRIN-INAF 2016

The Cradle of Life - GENESIS-SKA (General Conditions in Early Planetary Systems for the rise of life with SKA). I.M. acknowledges the financial support of the Government of Comunidad Autónoma de Madrid (Spain) through a "Talento" Fellowship (2016-T1/TIC-1890). Based on observations collected at the Centro Astronómico Hispano Alemán (CAHA) at Calar Alto, operated jointly by the Max-Planck Institut für Astronomie and the Instituto de Astrofísica de Andalucía (CSIC). This work has made use of data from the European Space Agency (ESA) mission *Gaia* (<https://www.cosmos.esa.int/gaia>), processed by the *Gaia* Data Processing and Analysis Consortium (DPAC, <https://www.cosmos.esa.int/web/gaia/dpac/consortium>). Funding for the DPAC has been provided by national institutions, in particular the institutions participating in the *Gaia* Multilateral Agreement.

References

- Aceituno, J., Sánchez, S. F., Grupp, F., et al. 2013, *A&A*, 552, A31
 Andrews, S. M., Wilner, D. J., Espaillat, C., et al. 2011, *ApJ*, 732, 42
 Baraffe, I., Chabrier, G., Barman, T. S., Allard, F., & Hauschildt, P. H. 2003, *A&A*, 402, 701
 Benisty, M., Juhasz, A., Boccaletti, A., et al. 2015, *A&A*, 578, L6
 Beskrovnaya, N. G., Pogodin, M. A., Miroshnichenko, A. S., et al. 1999, *A&A*, 343, 163
 Beuzit, J.-L., Feldt, M., Dohlen, K., et al. 2008, in *Proc. SPIE*, Vol. 7014, Ground-based and Airborne Instrumentation for Astronomy II, 701418
 Biller, B. A., Males, J., Rodigas, T., et al. 2014, *ApJ*, 792, L22
 Boccaletti, A., Pantin, E., Lagrange, A.-M., et al. 2013, *A&A*, 560, A20
 Boehler, Y., Ricci, L., Weaver, E., et al. 2017, *ArXiv e-prints* [arXiv:1712.08845]
 Bowler, B. P., Liu, M. C., Kraus, A. L., & Mann, A. W. 2014, *ApJ*, 784, 65
 Castelli, F. & Kurucz, R. L. 2003, in *IAU Symposium*, Vol. 210, Modelling of Stellar Atmospheres, ed. N. Piskunov, W. W. Weiss, & D. F. Gray, A20
 Chapillon, E., Guilloteau, S., Dutrey, A., & Piétu, V. 2008, *A&A*, 488, 565
 Chauvin, G., Lagrange, A.-M., Beust, H., et al. 2012, *A&A*, 542, A41
 Close, L. M., Follette, K. B., Males, J. R., et al. 2014, *ApJ*, 781, L30
 Dong, R., Zhu, Z., Rafikov, R. R., & Stone, J. M. 2015, *ApJ*, 809, L5
 Fairlamb, J. R., Oudmaijer, R. D., Mendigutía, I., Ilee, J. D., & van den Ancker, M. E. 2017, *MNRAS*, 464, 4721
 Gaia Collaboration, Brown, A. G. A., Vallenari, A., et al. 2016a, *A&A*, 595, A2
 Gaia Collaboration, Prusti, T., de Bruijne, J. H. J., et al. 2016b, *A&A*, 595, A1
 Grady, C. A., Muto, T., Hashimoto, J., et al. 2013, *ApJ*, 762, 48
 Gullbring, E., Hartmann, L., Briceño, C., & Calvet, N. 1998, *ApJ*, 492, 323
 Huélamo, N., Lacour, S., Tuthill, P., et al. 2011, *A&A*, 528, L7
 Isella, A., Natta, A., Wilner, D., Carpenter, J. M., & Testi, L. 2010, *ApJ*, 725, 1735
 Kraus, A. L. & Ireland, M. J. 2012, *ApJ*, 745, 5
 Kurucz, R. 1993, *SYNTHES Spectrum Synthesis Programs and Line Data*. Kurucz CD-ROM No. 18. Cambridge, Mass.: Smithsonian Astrophysical Observatory, 1993., 18
 Lafrenière, D., Marois, C., Doyon, R., Nadeau, D., & Artigau, É. 2007, *ApJ*, 660, 770
 Ligi, R., Vigan, A., Gratton, R., et al. 2018, *MNRAS*, 473, 1774
 Marino, S., Casassus, S., Perez, S., et al. 2015, *ApJ*, 813, 76
 Marois, C., Lafrenière, D., Doyon, R., Macintosh, B., & Nadeau, D. 2006, *ApJ*, 641, 556
 Mawet, D., Milli, J., Wahhaj, Z., et al. 2014, *ApJ*, 792, 97
 Mayama, S., Hashimoto, J., Muto, T., et al. 2012, *ApJ*, 760, L26
 Meeus, G., Montesinos, B., Mendigutía, I., et al. 2012, *A&A*, 544, A78
 Mendigutía, I., Calvet, N., Montesinos, B., et al. 2011, *A&A*, 535, A99
 Mendigutía, I., Oudmaijer, R. D., Garufi, A., et al. 2017, *A&A*, 608, A104
 Patat, F., Moehler, S., O'Brien, K., et al. 2011, *A&A*, 527, A91
 Pérez, L. M., Carpenter, J. M., Andrews, S. M., et al. 2016, *Science*, 353, 1519
 Pinilla, P., de Boer, J., Benisty, M., et al. 2015, *A&A*, 584, L4
 Pohl, A., Benisty, M., Pinilla, P., et al. 2017, *ApJ*, 850, 52
 Quanz, S. P., Amara, A., Meyer, M. R., et al. 2013, *ApJ*, 766, L1
 Racine, R., Walker, G. A. H., Nadeau, D., Doyon, R., & Marois, C. 1999, *PASP*, 111, 587
 Reggiani, M., Christiaens, V., Absil, O., et al. 2017, *ArXiv e-prints* [arXiv:1710.11393]
 Rieke, G. H. & Lebofsky, M. J. 1985, *ApJ*, 288, 618
 Rigliaco, E., Natta, A., Testi, L., et al. 2012, *A&A*, 548, A56
 Sallum, S., Follette, K. B., Eisner, J. A., et al. 2015, *Nature*, 527, 342
 Schmid, H. M., Bazzon, A., Milli, J., et al. 2017, *A&A*, 602, A53
 Soummer, R., Pueyo, L., & Larkin, J. 2012, *ApJ*, 755, L28
 Thalmann, C., Schmid, H. M., Boccaletti, A., et al. 2008, in *Proc. SPIE*, Vol. 7014, Ground-based and Airborne Instrumentation for Astronomy II, 70143F
 van Leeuwen, F. 2007, *A&A*, 474, 653
 Whelan, E. T., Huélamo, N., Alcalá, J. M., et al. 2015, *A&A*, 579, A48
 Zhou, Y., Herczeg, G. J., Kraus, A. L., Metchev, S., & Cruz, K. L. 2014, *ApJ*, 783, L17
 Zhu, Z. 2015, *ApJ*, 799, 16